

2025 | 495

## Research and multi-objective optimization of fuel cavitation flow inside fuel injector control valve

Fuel Injection & Gas Admission and Engine Components

Jiangtao Li, Wuhan university of technology

Yuhai He, Wuhan University of Technology  
Zhenming Liu, Naval University of Engineering  
Kai Song, Wuhan University of Technology  
Xianlin Wan, Wuhan University of Technology  
Boyang Sun, Wuhan University of Technology

---

This paper has been presented and published at the 31st CIMAC World Congress 2025 in Zürich, Switzerland. The CIMAC Congress is held every three years, each time in a different member country. The Congress program centres around the presentation of Technical Papers on engine research and development, application engineering on the original equipment side and engine operation and maintenance on the end-user side. The themes of the 2025 event included Digitalization & Connectivity for different applications, System Integration & Hybridization, Electrification & Fuel Cells Development, Emission Reduction Technologies, Conventional and New Fuels, Dual Fuel Engines, Lubricants, Product Development of Gas and Diesel Engines, Components & Tribology, Turbochargers, Controls & Automation, Engine Thermodynamics, Simulation Technologies as well as Basic Research & Advanced Engineering. The copyright of this paper is with CIMAC. For further information please visit <https://www.cimac.com>.

## ABSTRACT

High-speed and high-power diesel engines have become an important development direction of modern naval diesel engines due to high injection pressure, short injection time and high speed. Although high-pressure common rail technology improves the economy, high injection pressure leads to the increasingly serious problem of injector cavitation. Cavitation not only reduces the flow cross section of the control valve and affects the fuel flow, but also leads to the shedding of the valve inner wall material, which affects the sealing performance and injection precision, and then seriously affects the reliability of the injector control valve.

This paper adopts a combination of fluid numerical calculations and visualization experiments to study the fuel flow characteristics, cavitation influencing factors and evolution mechanism of the injector control valve. The influence of the dynamic working process and structural parameters of the control valve on the fuel cavitation flow, as well as the changes in the distribution of the cavitation field, mass flow rate and gas volume fraction in the key parts, are discussed in depth.

Firstly, a static simulation model of the fuel injector control valve was established, and the reliability of the model was verified using static operating condition experimental data. The effects of different structural parameters on the cavitation phenomenon of the control valve were investigated by changing the inlet angle of the control valve ball valve seat, the diameter of the outlet hole and the length of the outlet hole. It is found that the selection of the appropriate ball valve seat inlet angle can effectively guide the location of cavitation formation, development and collapse in the ball valve cavity to achieve the effect of reducing the degree of control valve cavitation. Then, the control valve model was further constructed and optimized based on a framework combining artificial intelligence methods and physical numerical calculation models. The dynamic calculation results before and after the optimization of the control valve structure are studied comparatively, indicating that the optimized control valve model can achieve the effect of suppressing the cavitation phenomenon of the control valve and improving the fuel control performance of the control valve.

**Keywords:** Injector control valve, Fuel cavitation flow, Numerical calculation, Artificial intelligence.

## 1 INTRODUCTION

Diesel engines, with their high thermal efficiency, large output power, and reliable performance, are widely used in civilian facilities, transportation, and national defense military equipment [1] [2]. To optimize diesel engine performance, high-pressure common rail technology has been widely adopted [3] [4]. The introduction of high-pressure common rail technology enhances fuel atomization and combustion completeness, thereby improving engine efficiency while advancing energy conservation and emission reduction goals [5]. As a core component of HPCR systems, the fuel injector control valve plays a pivotal role in regulating fuel injection timing and pressure with micrometer-level precision. However, under extreme pressure differential, the fuel flow within the control valve undergoes complex multiphase transitions, triggering cavitation phenomena that critically compromise valve durability and injection accuracy [6] [7].

Cavitation in control valves arises from localized pressure drops below the fuel's vaporization threshold, generating vapor bubbles that collapse violently upon entering high-pressure regions [8]. This process induces erosive microjets capable of damaging critical components such as the guide hole surfaces, ball valve seats, and sealing interfaces (Fig. 1). Such damage not only accelerates wear but also disrupts the valve's dynamic response, leading to unstable fuel delivery and degraded combustion performance [9]. Furthermore, cavitation-induced flow instabilities create feedback challenges for electronic control units (ECUs), hindering precise pressure modulation [10]. Therefore, to reduce the cavitation phenomenon inside the control valve, the formation and development mechanisms of cavitation need to be further investigated. Thus, the study of fuel flow, phase transition and cavitation in injector control valves is of great scientific significance and practical value.

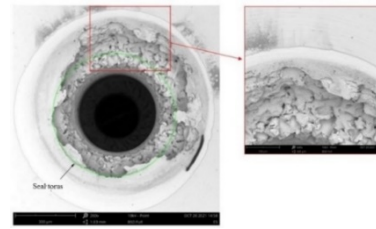


Figure 1 Electronic microscope scan of ball valve's surface cavitation

In recent years, the cavitation phenomenon in nozzles has been widely considered and studied, while the cavitation phenomenon in control valves has been relatively less studied, while the cavitation phenomenon in nozzles is similar to that in control valves, which is the cavitation flow of fuel in microchannels. Domestic and foreign researchers have investigated cavitation in nozzles and control valves through visualization tests and numerical simulations.

The experimental study of cavitation phenomena within microchannels generally adopts a visualization approach. In 2001, Winklhofer et al. [11] conducted experiments to investigate the flow and cavitation phenomena within nozzle microchannels, with the microchannel geometry depicted in Figure 2. Their research documented the transition from liquid to vapor flow and the interaction between liquid flow patterns and cavitation gas forms. They measured the distribution of vapor fields, liquid pressure fields, and velocities, providing precise and comprehensive records of the flow phenomena involved in cavitation flow. Ma et al. [12] performed experimental and numerical simulations for 2D visualization of control valves and validated the simulation methods and models. They proposed a new structural design of the control valve called the convergent model. They compared the original model and the converged model at different lifts through 3D simulations and found that lamellar cavitation occurs on the sealing cone and ball surfaces, and the cavitation intensity increases

with the increase of lift. Liu et al. [13] revealed the mechanism of the influence of injection pulse width, rail pressure and valve lift on the cavitation behavior of control valves through dynamic working condition simulation. It was showed that the cavitation intensity of the control and guide orifices was not sensitive enough to the above parameters, the shorter the pulse width, the more severe the average cavitation in the ball valve cavity, the increase of rail pressure and the increase of ball valve lift would aggravate the cavitation, and the location of the cavitation would be shifted forward and closer to the sealing annular surface. Chao et al. [14] investigated the flow and cavitation phenomena in a control valve by numerical simulation and studied in detail the effects of the structural parameters of the control valve on the flow and cavitation. They found that not only the variation of pressure but also velocity is an important factor affecting cavitation. An increase in flow velocity decreases the pressure within the flow field, thus intensifying the development of cavitation. As the cavitation region increases, fuel flow is impeded and the flow velocity decreases. However, the decrease in flow velocity in turn inhibits the development of cavitation.

Cao et al. [15] conducted visualization experiments in an enlarged optical nozzle to study the cavitation characteristics of the nozzle and their impact on spray characteristics. They found that vortex cavitation is one of the most significant factors influencing pressure fluctuations in the injection system and that the spray cone angle increases proportionally with the development of vortex cavitation. Zhang et al. [16] also studied the influence of fuel temperature on the internal flow of the nozzle and spray atomization through visualization experiments. They used transparent acrylic model nozzles, enlarged 10 times and with different geometries, to study flow visualization and employed high-speed digital cameras to capture the flow phenomena in the sac chamber and nozzle area. They use experimental methods

to analyze the impact of the nozzle sac volume structure on the internal cavitation flow of the nozzle and subsequent spray. They found that the flow characteristics within the nozzle and spray formation are sensitive to fuel temperature.

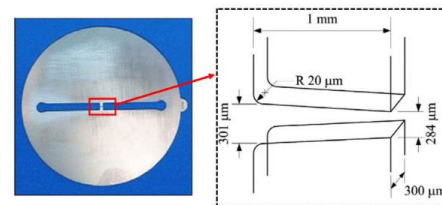


Figure 2 Microchannel Geometry

With the development of numerical simulation technology, researchers have also utilized computational fluid dynamics (CFD) and other methods to simulate the cavitation flow within nozzles. Wang et al. [17] proposed a coupled simulation method for spray and nozzle cavitation flow and verified the accuracy of the model through experiments. This spray-coupled simulation method adopts the Eulerian method for the flow within the nozzle and the Lagrangian method for the spray, fully considering the influence of nozzle cavitation flow on the primary breakup process of the spray near the nozzle orifice. They found that the simulation results obtained by coupling this model with nozzle flow rates are closer to the experimental spray contours.

Yu et al. [18] used numerical simulation methods through the OpenFOAM software to study the impact of cavitation phenomena within injector nozzles on spray morphology. They found that flow separation, wall shear, and cavitation within the nozzle are the main causes of jet breakup and that the combined effect of wall shear and cavitation in cavitation simulations results in higher jet breakup intensity and a wider spray range compared to non-cavitation simulations that only experience wall shear. He et al. [19] established a flow visualization experimental system for the transparent and enlarged porous injector nozzle tip.

They compared and validated it with the results of three-dimensional numerical simulations of cavitation flow within the injector under a mixed multiphase cavitation flow model. They found that numerical simulations of the nozzle using ANSYS Fluent can reveal the three-dimensional nature of the nozzle flow and the location and shape of cavitation-induced vapor distribution, which aids in a better understanding of nozzle flow and ultimately proposes optimization ideas for the injector. Koukouvinis et al. [20] studied the development of cavitation-induced erosion within engine injectors through numerical simulations and X-ray CT scanning. They compared the numerical simulation results with X-ray scanning results, which used large eddy simulations and a two-phase homogeneous mixture model. They found that the location of the pressure peaks in the numerical simulations agreed well with the actual erosion locations identified by X-ray scanning.

Studies have shown that pressure fluctuations within the nozzle influence the cavitation phenomenon within the microchannel of a nozzle. Dai et al. [21] studied the dynamics and cavitation characteristics of the internal flow within a nozzle under different injection pressures and throttling intensities. They conducted a visualization study of the internal flow within the nozzle using high-speed imaging technology. The research results revealed that as the needle lift increases, the initial cavitation rate increases due to the increase in liquid pressure. With further increases in needle lift, the cavitation rate decreases due to the weakening of the throttling effect. When the injection needle lift is constant, cavitation rapidly intensifies with increasing injection pressure and remains unchanged.

The geometric structure of the nozzle microchannel also has a certain impact on the cavitation phenomenon of fuel within the microchannel. Molina et al. [22] studied the effects of four nozzles with different elliptical orifices and one standard circular orifice nozzle on the internal

flow and the development of cavitation. The results indicated that cavitation is less likely to occur in nozzles with elliptical orifices where the major axis is vertically oriented, and these nozzles have lower flow coefficients. Conversely, nozzles with elliptical orifices where the major axis is horizontally oriented are more prone to cavitation and have higher flow coefficients. Chen et al. [23] conducted experimental studies on the impact of nozzle geometry on nozzle cavitation and spray characteristics. They used a high-speed camera with a long-distance microscope to capture transient cavitation flows and spray characteristics in an optical nozzle. The agglomeration phenomena of geometrically induced cavitation were visually captured and analyzed. The study found that cavitation within the nozzle excites instability in the spray cone angle, and the influence of geometrically induced cavitation on the spray cone angle is very significant. Additionally, the length-to-diameter ratio and the nozzle's sac shape significantly affect both cavitation and spray characteristics. Cui et al. [24] conducted visualization experiments on the internal flow of nozzles and studied the impact of the nozzle's taper, inclination angle, and diameter errors on atomization. The results showed that cylindrical nozzles with smaller diameters inhibit the development of cavitation, and convergent nozzles have the greatest impact on the cavitation and atomization processes. Divergent nozzles perform better at lower pressures.

In summary, domestic and foreign researchers have studied the cavitation flow characteristics within engine control valves and nozzles to varying degrees. On the one hand, cavitation can lead to a decrease in system control accuracy and cause problems such as cavitation erosion, noise and vibration. On the other hand, cavitation also affects the fuel injection characteristics to some extent. This research project primarily focuses on the study of cavitation phenomena within fuel injector control valves, mainly including the influence of structural parameters such as the length of the

control valve's guide hole, the length of the oil supply hole, the diameter of the oil supply hole, the diameter of the sealing ball, and the cone angle of the ball valve seat on the cavitation phenomenon within the control valve. By optimizing these structural parameters, the project aims to explore effective control methods for fuel cavitation within the control valve to improve the injection system's control accuracy and operational stability.

## 2 MODEL AND METHOD

### 2.1 Mathematical Model

#### 2.1.1 Multiphase Flow Model

This paper selects the Volume of Fluid (VOF) model to describe the fuel cavitation flow within the control valve. The governing equations of the VOF model mainly include the volume fraction, momentum, and energy.

##### (1) Volume Fraction Equation:

The interface between phases was tracked by solving the continuity equation for the volume fraction of one (or more) phases. For the  $q$ -th phase, the volume fraction equation has the following form:

$$\frac{1}{\rho_q} \left[ \frac{\partial}{\partial t} (\alpha_q \rho_q) + \nabla \cdot (\alpha_q \rho_q \vec{v}_q) \right] = S_{\alpha_q} + \sum_{p=1}^n (\dot{m}_{pq} - \dot{m}_{qp}) \quad (1)$$

Where  $\dot{m}_{pq}$  is the mass transfer from  $p$ -phase to  $q$ -phase, and  $\dot{m}_{qp}$  is the mass transfer from  $q$ -phase to  $p$ -phase.

The following formula calculates the volume equation for the initial phase:

$$\sum_{q=1}^n \alpha_q = 1 \quad (2)$$

The following formula can solve the volume fraction equation:

$$\frac{\alpha_q^{n+1} \rho_q^{n+1} - \alpha_q^n \rho_q^n}{\Delta t} V + \sum_f (\rho_q^{n+1} U_f^{n+1} \alpha_{q,f}^{n+1}) = \left[ S_{\alpha_q} + \sum_{p=1}^n (\bar{m}_{pq} - \bar{m}_{qp}) \right] V \quad (3)$$

Where  $n+1$  is the current time step index.  $n$  is the previous time step index,  $\alpha_q^{n+1}$  is the cell volume

fraction at step  $n+1$ ,  $\alpha_q^n$  is the cell volume fraction

at time step  $n$ ,  $\alpha_{q,f}^{n+1}$  is the surface value of the

volume fraction at time step  $n+1$ ,  $U_f^{n+1}$  is the volume flux through the surface at time step  $n+1$ , and  $V$  is the cell volume.

(2) The following equation can calculate the momentum equation:

$$\frac{\partial}{\partial t} (\rho \vec{v}) + \nabla \cdot (\rho \vec{v} \vec{v}) = -\nabla p + \nabla \cdot [\mu (\nabla \vec{v} + \nabla \vec{v}^T)] + \rho \vec{g} + \vec{F} \quad (4)$$

(3) The following equation can calculate the energy equation:

$$\frac{\partial}{\partial t} (\rho E) + \nabla \cdot (\vec{v} (\rho E + p)) = \nabla \cdot \left( k_{eff} \nabla T - \sum_q \sum_j h_{j,q} \vec{J}_{j,q} + (\vec{\tau}_{eff} \cdot \vec{v}) \right) + S_h \quad (5)$$

Where  $k_{eff}$  is the effective conductivity,  $\vec{J}_j$  is the diffusive flux of species  $j$ ,  $h_{j,q}$  is the enthalpy of species  $j$  in phase  $q$ , and  $\vec{J}_{j,q}$  is the diffusive flux

of species  $j$  in phase  $q$ . The first three terms on the right side of the equation represent the energy transfer due to conduction and viscous dissipation, respectively. The first three terms on the right-hand side of the equation represent the energy transfer due to conduction, species diffusion, and viscous

dissipation, respectively.  $S_h$  is the defined volumetric heat source.

### 2.1.2 Turbulence model

For turbulent flow, there are three types of numerical computation methods: Reynolds time-averaged method (RANS), large eddy simulation (LES), and direct numerical simulation (DNS). DNS requires huge computing resources, which are difficult to realize on a single workstation. The large eddy simulation is between DNS and RANS, the computational accuracy is higher than RANS, and the computational cost is lower than direct numerical simulation. Therefore, considering the computational accuracy and price, this paper selects the large eddy simulation model for turbulence calculation.

Among the LES models are four sub-grid scale models: the Smagorinsky-Lilly model, the dynamic Smagorinsky-Lilly model, the WALE model, and the dynamic kinetic energy sub-grid scale model. The subgrid sub-model used in this study is the WALE model [22], whose subgrid-scale turbulent stresses are calculated as follows:

$$\tau_{ij} - \frac{1}{3}\tau_{kk}\delta_{ij} = -2\mu_t\bar{S}_{ij} \quad (6)$$

$$\bar{S}_{ij} = \frac{1}{2} \left( \frac{\partial \bar{u}_i}{\partial x_j} + \frac{\partial \bar{u}_j}{\partial x_i} \right) \quad (7)$$

Where  $\mu_t$  is the turbulent viscosity at the subgrid scale,  $\tau_{kk}$  is the isotropic part of the stress at the subgrid scale, and  $\bar{S}_{ij}$  is the strain rate tensor at the resolved scale.

In the WALE model, the eddy viscosity modeled as:

$$\mu_t = \rho L_s^2 \frac{(S_{ij}^d S_{ij}^d)^{3/2}}{(\bar{S}_{ij} \bar{S}_{ij})^{5/2} + (S_{ij}^d S_{ij}^d)^{5/4}} \quad (8)$$

$$L_s = \min(\kappa d, C_w V^{1/3}) \quad (9)$$

$$S_{ij}^d = \frac{1}{2}(\bar{g}_{ij}^2 + \bar{g}_{ij}^2) - \frac{1}{3}\delta_{ij}\bar{g}_{kk}^2, \bar{g}_{ij} = \frac{\partial \bar{u}_i}{\partial x_j} \quad (10)$$

Where  $\kappa$  is the von Karmen constant, 0.41,  $C_w$  is the WALE model constant, 0.5.  $L_s$  is the subgrid-scale mixing length, and  $d$  is the distance to the nearest wall.

### 2.1.3 Cavitation model

The commonly used cavitation models are mainly the Zwart-Gerber-Belamri (ZGB) cavitation model and the Schnerr-Sauer (SS) cavitation model. The ZGB cavitation model can accurately describe the initial radius of bubbles, the volume fraction of gas nuclei, etc., and the simulation results are closer to reality. In addition, the ZGB cavitation model can capture many details of the cavitation process, such as the development of cavitation, bubble generation, and collapse. This makes the model more accurate in studying and understanding cavitation phenomena. Therefore, the ZGB cavitation model is chosen for simulation.

The ZGB cavitation model assumes that all bubbles in the system have the same dimensions, and the total interphase mass transfer rate  $R$  per unit volume is calculated using the bubble number density  $n$ . The mass transfer rate  $R$  per unit volume is calculated using the bubble number density. The rate of mass change for a single bubble is calculated as follows:

$$R = n \times \left( 4\pi \mathfrak{R}_B^2 \rho_v \frac{D\mathfrak{R}_B}{Dt} \right) \quad (11)$$

The relationship between the vapor volume fraction  $\alpha$  and the bubble number density  $n_b$ , and bubble radius  $\mathfrak{R}_B$  is as follows:



$$\alpha = n \times \left( \frac{4}{3} \pi \mathfrak{R}_B^3 \right) \quad (12)$$

Combining the above two equations yields an expression for the net mass transfer:

$$R = \frac{3\alpha\rho_v}{\mathfrak{R}_B} \sqrt{\frac{2}{3} \frac{P_B - P}{\rho_l}} \quad (13)$$

The above equation is derived under the assumption of bubble growth (evaporation), and to apply it to the process of bubble bursting (condensation), the following generalized equation is used for the calculation:

$$R_e = F \frac{3\alpha\rho_v}{\mathfrak{R}_B} \sqrt{\frac{2}{3} \frac{|P_B - P|}{\rho_l}} \text{sign}(P_B - P) \quad (14)$$

Where  $F$  is the empirical calibration factor.

While the above equation can be applied well to the condensation process, it contains some errors in its description of the evaporation process, mainly because it is assumed in the calculations that the bubbles do not interact. It is accurate only at the earliest stages of cavitation when the cavitation bubbles grow from the nucleation site. As the volume fraction of the gas phase increases, the density of the nucleation sites decreases accordingly. Zwart-Gerber-Belamri proposed a correction using  $\alpha_{nuc} (1 - \alpha_v)$  instead of  $\alpha_v$  to model this process accurately. The final cavitation model is calculated as follows:

When  $P \leq P_v$

$$R_e = F_{vap} \frac{3\alpha_{nuc} (1 - \alpha_v) \rho_v}{\mathfrak{R}_B} \sqrt{\frac{2}{3} \frac{P_v - P}{\rho_l}} \quad (15)$$

When  $P \geq P_v$

$$R_e = F_{cond} \frac{3\alpha_v \rho_v}{\mathfrak{R}_B} \sqrt{\frac{2}{3} \frac{P - P_v}{\rho_l}} \quad (16)$$

Where  $P$  is the local pressure of the flow field,  $P_v$  is the saturated vapor pressure,  $\mathfrak{R}_B$  is the radius of the bubble, with a value of  $10^{-6}$ ,  $\alpha_{nuc}$  is the volume fraction of nucleation sites, with a value of  $5 \times 10^{-4}$ ,  $F_{vap}$  is the evaporation coefficient, with a value of 50, and  $F_{cond}$  is the condensation coefficient, with a value of 0.01.  $\rho_v$  and  $\rho_l$  are the gas-phase density and liquid-phase density, respectively.

## 2.2 Model Validation

In order to verify the accuracy of the selected model, the simulation results were analyzed in comparison with the experimental results of Winkelhofer et al. [11]. The fuel physical parameters used in the simulations are shown in Table 1. In this study, the inlet condition of the microchannel numerical model was set to pressure inlet, and the outlet condition was set to pressure outlet. The pressure at the inlet was kept constant at 10 MPa, and the outlet pressure was set in the range of 1.9 to 8.5 MPa to facilitate the study of fuel cavitation flow characteristics at different pressure drops.

Table 1 Fuel Physical Parameters

Fuel Physical Parameters	value
liquid-phase density ( $\text{kg} \cdot \text{m}^{-3}$ )	830
Liquid phase dynamic viscosity ( $\text{kg} \cdot \text{m}^{-1} \cdot \text{s}^{-1}$ )	0.0024
Saturated vapor pressure (Pa)	2000
Vapor density ( $\text{kg} \cdot \text{m}^{-3}$ )	0.029
Vapor-phase dynamic viscosity ( $\text{kg} \cdot \text{m}^{-1} \cdot \text{s}^{-1}$ )	$3.1 \times 10^{-6}$
Temperature ( $^{\circ}\text{C}$ )	20

Figure 3 shows the experimental and simulated outlet mass flow rate data at different differential pressures. Figure 4 shows the experimental and simulated fluid flow velocity distribution values over the microchannel cross section. The comparison curves in the figures show that the computational results of the model selected for this study are in better agreement with the experimental results of



Winklhofer et al. [11], and the error is within 5%. Table 2 shows the experimental and simulated images of the microchannel cavitation distribution at inlet and outlet pressure differences of 8 MPa. It can be seen that the cavitation distribution regions in the experiment and simulation are in good agreement. It further proves the accuracy of the established model.

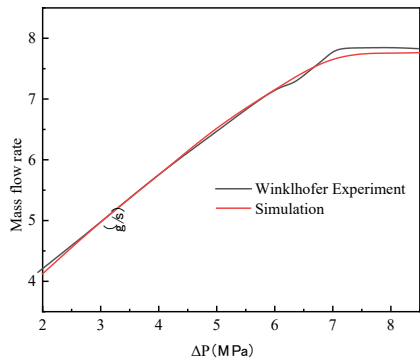


Figure 3 Outlet mass flow rate at different differential pressures

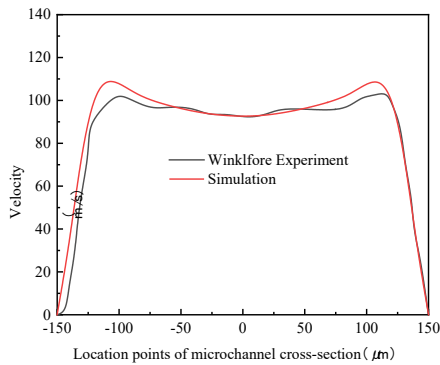
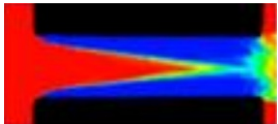
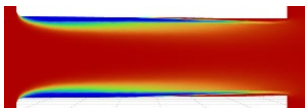


Figure 4 Flow velocity in microchannel cross section

Table 2 Comparison of cavitation images

$\Delta P=8\text{MPa}$	
Winklhofer experiment	
Simulation	

### 2.3 Control valve model structure and mesh

This paper focuses on the influence of the

structural parameters of the flow path of a control valve on the cavitation characteristics. The three-dimensional static model of the control valve is shown in Figure 5. The lower end is the ball valve inlet, and the upper is the outlet. Under the boundary conditions that the inlet pressure is 200 MPa, and the outlet pressure is atmospheric, the effects of different structural parameters, such as the chamfer of the ball valve, the lift of the ball, the diameter of the ball, the length of the pilot hole, the diameter of the pilot hole, and the length of the oil supply hole, on the internal cavitation characteristics of the regulating valve are considered separately. The initial size parameters of the ball valve model are shown in Table 3.

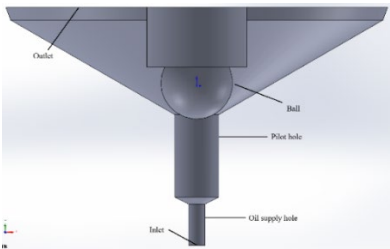


Figure 5 3D statical model of control valve

Table 3 Dimensional parameters of the control valve model

Model structure	value
Chamfering angle (°)	120
Ball lift (mm)	0.05
Ball diameter (mm)	1.3
length of pilot hole (mm)	1.5
Diameter of pilot hole (mm)	0.8
Length of oil supply hole (mm)	0.75

In this study, ICEM software is used to mesh the hexahedral structure of the control valve model. To ensure meshing quality, the geometry was first cleaned up and optimized to ensure that critical features such as ball seat contact surfaces and sealing gaps could be accurately identified and treated. Mesh encryption was performed in critical areas such as ball valve gaps. The mesh model of the initial structure ball valve model is shown in

Figure 6, with a total number of 5.62 million meshes and a Taylor scale estimated to be about  $3\text{ }\mu\text{m}$ . In addition, six groups of meshes, 1.2 million, 2.02 million, 3.06 million, 4.26 million, 5.62 million, and 6.71 million, are respectively divided for the validation of mesh independence. The mass flow rate at the ball valve outlet is monitored, and the validation results are shown in Figure 7. It can be seen that before the number of grid nodes reaches 3 million, the outlet mass flow rate varies greatly. After the number of grid nodes exceeds 3 million, there is a small range of fluctuation in the mass flow rate of the ball valve outlet. When the number of grid nodes exceeds 5 million, the mass flow rate of the ball valve outlet is almost unchanged and is not affected by the number of grid nodes. To ensure the calculation accuracy, 5.62 million grids were selected for calculation in this study.

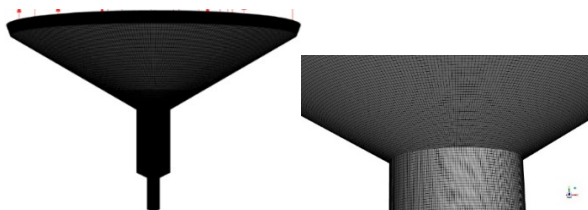


Figure 6 Mesh model of the initial structure ball valve model

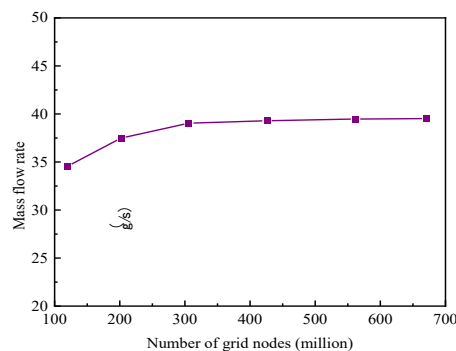


Figure 7 Mass flow rate for different grids

## 2.4 Numerical calculation setup

During the numerical calculation of the model, the working reference pressure was set to one atmosphere, the fuel inlet pressure was set to 200 MPa, and the outlet pressure was set to 0 MPa. The physical parameters of the fuel are the same

as in the previous section. The VOF model was selected for the multiphase flow model, the large eddy simulation (LES) model for the turbulence model, and the ZGB model for the cavitation model. The pressure-velocity coupling method is set as SIMPLEC; the pressure solution format is PRESTO! Format; the gradient solution format is Least Squares Cell Based format; the momentum and volume fraction solution format is the second-order windward format, and the time term discretization format is the first-order windward format. The model is solved on a 64-core, 128-thread high-performance workstation.

## 3 RESULTS AND DISCUSSION

### 3.1 Effect of ball valve seat cone angle on cavitation

The ball valve seat cone angle affects the diesel flow rate and flow direction, changing the cavitation state inside the ball valve. Figure 8 shows the cavitation distribution under four cone angles ( $110^\circ$ ,  $120^\circ$ ,  $130^\circ$ ,  $140^\circ$ ). It can be seen that at  $110^\circ$ , the cavitation extends backward close to the seat wall, and there are cavitation bubbles on the lower wall surface. At  $120^\circ$ , the cavitation area near the sealing ball is reduced. At  $130^\circ$ , the cavitation phenomenon increases significantly, and the cavitation in the lower guide hole is reduced. At  $140^\circ$ , there is even less cavitation in the guide hole, and the cavitation area in the ball valve cavity is far away from the wall surface. Figure 9 shows the flow velocity distribution, with a low velocity region near the bottom of the sealing ball and the entrance to the ball valve cavity, due to flow obstruction near the fuel flow through to the sealing surface of the ball valve. At  $110^\circ$  and  $120^\circ$ , there are thin low velocity zones near the ball valve seat wall caused by flow separation. As the cone angle increases to  $130^\circ$  and  $140^\circ$ , the main flow moves away from the cone surface, and a low-pressure region forms near the high-velocity zone causing cavitation. Calculations revealed that the minimum gap cross-section flow velocities were 499.49 m/s and 489.91 m/s at  $110^\circ$  and  $120^\circ$ , respectively,

while they were 420.43 m/s and 406.20 m/s at 130° and 140°, respectively.

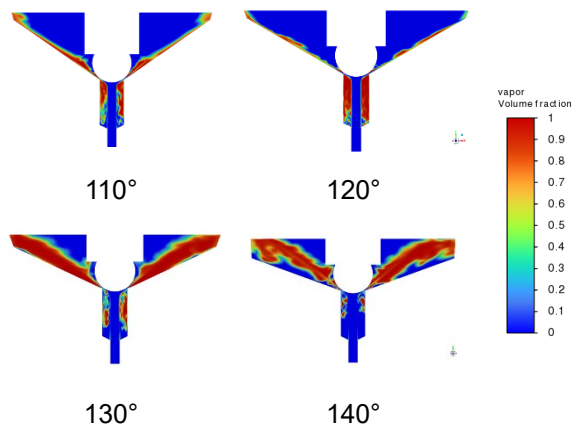


Figure 8 Cavitation pictures for different ball valve seat cone angles

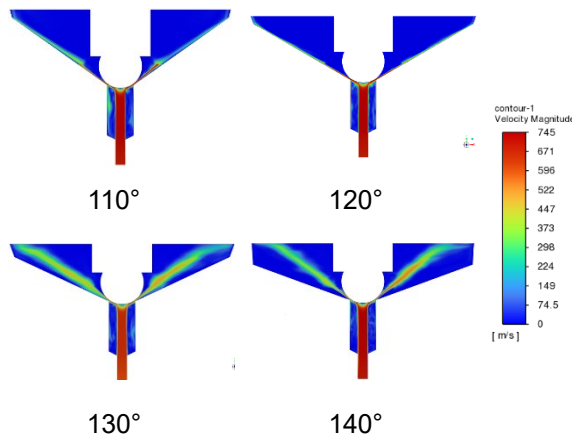


Figure 9 Flow velocity for different ball valve seat cone angles

Figure 10 illustrates the trend of mass flow rate and gas volume fraction at the minimum gap between the sealing ball and the wall for different ball valve seat cone angles. Both show a tendency to increase, then decrease, then increase again as the cone angle increases from 110° to 140°. Specifically, the gas volume fraction decreased to the lowest (0.29) at 130°, while the mass flow rate reached the highest (32.04 g/s) at 120°.

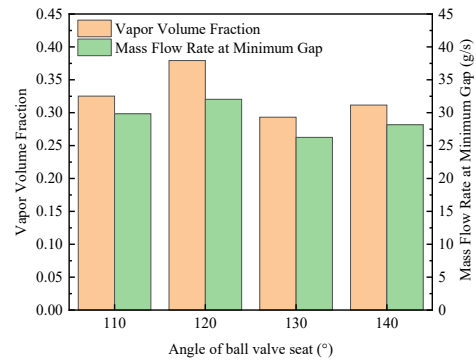


Figure 10 Mass flow rate and gas volume fraction at minimum gap for different ball valve seat cone angles

### 3.2 Effect of ball valve lift on cavitation

Figure 11 shows the cavitation cloud maps at different ball valve lifts. The cavitation region inside the ball valve cavity gradually decreases as the ball valve lift increases from 0.04 mm to 0.06 mm and slightly increases to 0.07 mm. The cavitation region near the inner wall of the pilot hole increases with the increase in lift. Figure 12 shows the flow velocity clouds at different ball valve lifts, and the main flow region moves towards the ball valve seat wall when the ball valve lift increases. When the lift is 0.04mm, the flow velocity in the center of the main stream area is high, resulting in a large cavitation area; when 0.05mm-0.07mm, the high velocity main stream is close to the wall, and the cavitation only occurs in the vicinity of the wall. Calculations found that the average flow velocity of the ball valve's minimum clearance cross-section increases with the lift increase, from 469.39m/s for 0.04mm to 564.53m/s for 0.07mm.

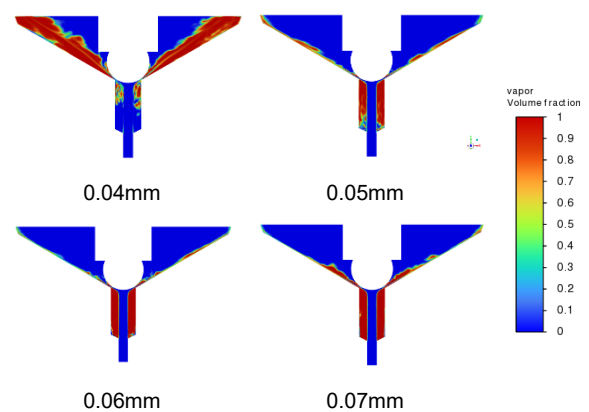


Figure 11 Cavitation pictures at different ball valve lifts

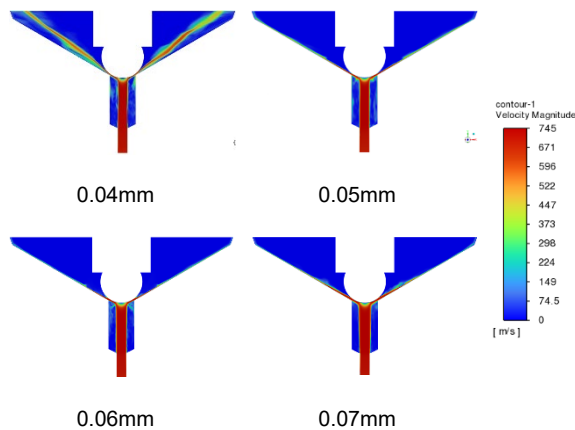


Figure 12 The flow velocity pictures at different ball valve lifts

Figure 13 shows the trend of mass flow rate and gas volume fraction at the minimum gap between the sealing ball and the wall at different ball valve lifts. With the increase of ball valve lift, the gas volume fraction in the critical region increases, while the mass flow rate at the minimum gap first increases and then decreases. Lift 0.04mm, the gas volume fraction is 0.21, and the mass flow rate is 29.30/s; lift 0.05mm, the gas volume fraction increases to 0.38, the mass flow rate increases to 34.13g/s; lift 0.06mm, the gas volume fraction continues to rise to 0.42 the mass flow rate reaches a peak value of 35.87g/s; lift At 0.07 mm, the gas volume fraction peaked at 0.58, but the mass flow rate decreased to 33.31g/s.

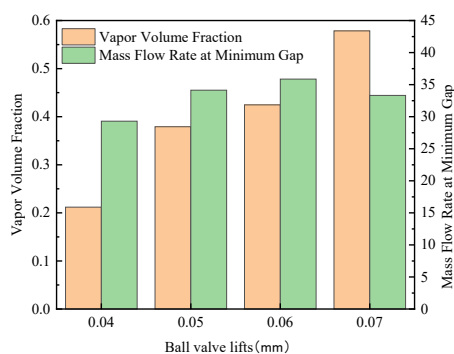


Figure 13 Mass flow rate and gas volume fraction at the minimum gap for different ball valve lifts

### 3.3 Effect of sealing ball diameter on cavitation

Figure 14 depicts the vapor volume fraction distribution within the ball valve corresponding to

four sealing ball diameters (1.2 mm, 1.3 mm, 1.5 mm, and 1.7 mm). Notably, cavitation intensity in the valve cavity exhibits a non-monotonic response to diameter variation: A 1.2-mm diameter configuration demonstrates the most severe cavitation in the valve cavity with negligible vapor formation near pilot hole walls. When increased to 1.3 mm, both cavity cavitation mitigation (proximal to sealing surfaces) and emerging wall-attached vapor clusters in pilot holes are observed. At larger diameters (1.5-1.7 mm), cavity vapor content stabilizes, whereas pilot hole wall cavitation escalates progressively, reaching peak severity at 1.7 mm.

Figure 15 quantifies the velocity field characteristics under identical diameter conditions. Increasing the sealing ball diameter induces systematic flow restructuring: The primary fuel jet migrates from proximal to the sealing ball toward the ball valve seat wall, thereby generating localized low-pressure zones adjacent to the jet core that trigger cavitation inception. Concomitantly, the cross-sectional average velocity in the minimum clearance region rises from 413.16 m/s (1.2 mm) to 531.81 m/s (1.7 mm), indicating a 28.7% enhancement attributable to geometric scaling.

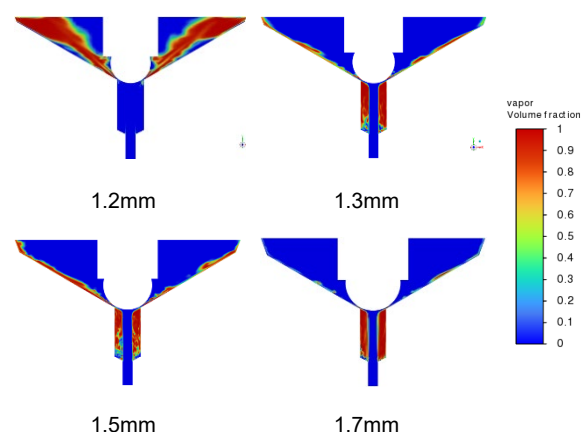


Figure 14 Cavitation pictures with different sealing ball diameters

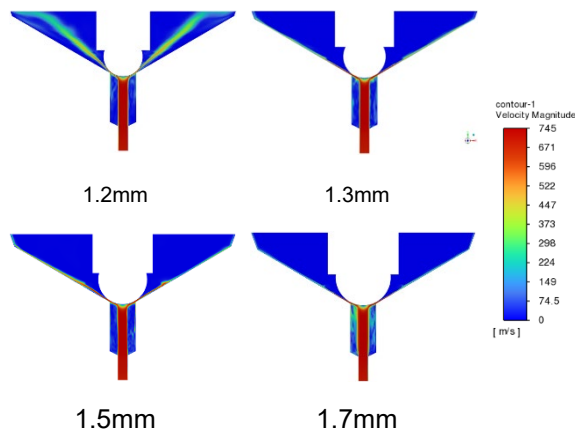


Figure 15 Flow velocity with different sealing ball diameters

Figure 16 shows the mass flow rate and gas volume fraction at the minimum gap for different sealing ball diameters. As the sealing ball diameter increased from 1.2 mm to 1.7 mm, the gas volume fraction in the critical region increased and then decreased, while the mass flow rate at the minimum gap increased and then decreased and then increased. Specifically, the gas volume fraction is 0.19 and the mass flow rate is 29.60g/s when the ball diameter is 1.2 mm; when the ball diameter is 1.3 mm, the gas volume fraction increases to 0.38, and the mass flow rate increases to 32.04 g/s; when the ball diameter is 1.5 mm, the gas volume fraction decreases slightly to 0.33, and the mass flow rate is 31.26 g/s; when the ball diameter is At 1.7 mm, the gas volume fraction decreases to 0.30 and the mass flow rate increases to 34.08 g/s.

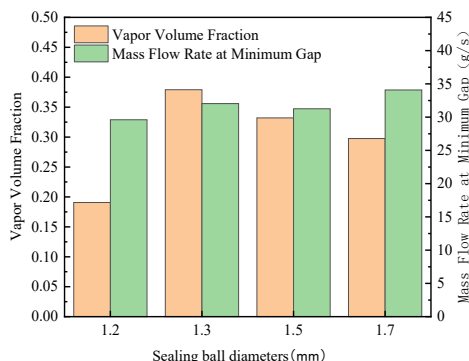


Figure 16 Mass flow rate and gas volume fraction at minimum gap for different sealing ball diameters

### 3.4 Effect of pilot hole length on cavitation

Figure 17 shows the cavitation pictures under different lengths of the pilot hole, the increase of the length of the pilot hole (from 0.5mm to 3.5mm), and the cavitation area in the upper part of the ball valve increasing and converging to the center. At 0.5mm and 1.5mm lengths, the cavitation area is almost the whole of the cavitation area near the inner wall of the pilot hole, and at 2.5mm and 3.5mm, the cavitation is mainly concentrated in the upper part. Figure 18 shows the velocity clouds under different guide hole lengths. The increase of guide hole length leads to the increase of fuel flow resistance, which makes the fuel flow rate decrease and the pressure drop increase when entering the ball valve cavity, so the local pressure near the fuel main stream area in the ball valve cavity is lower. The cavitation is more obvious under 2.5mm and 5mm guide hole lengths. The average flow velocity of the minimum clearance cross-section decreases with the increase of the length of the pilot hole, from 513.71m/s for 0.5mm to 465.57m/s for 3.5mm, because the long pilot hole increases the flow resistance.

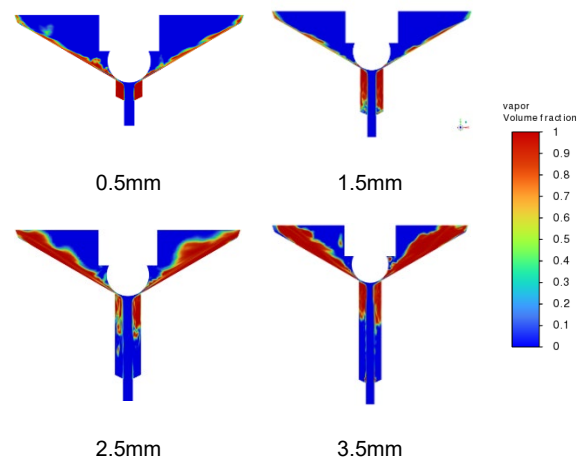
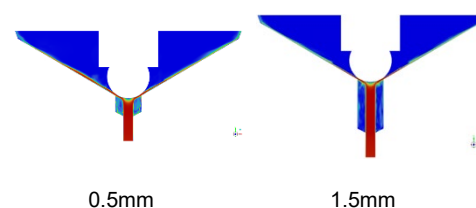


Figure 17 Cavitation pictures for different pilot hole lengths



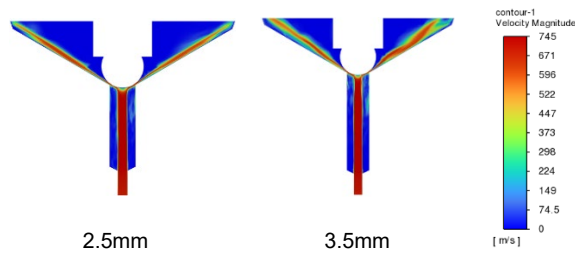


Figure 18 Flow velocity pictures with different guide hole lengths

Figure 19 shows the mass flow rate at the minimum gap and the gas volume fraction in the critical region of the ball valve for different pilot hole lengths. As the length of the pilot hole increases from 0.5 mm to 2.5 mm, the gas volume fraction in the critical zone and the mass flow rate at the smallest gap show a tendency to decrease, then increase, and then decrease. When the length of the guide hole is 0.5mm, 0.75mm, 2.5mm, and 3.5mm, the gas volume fraction in the critical region of the ball valve is 0.42, 0.3792, 0.40, and 0.3799, respectively. The mass flow rate at the minimum gap of the ball valve is 31.1g/s, 32.04g/s, 26.62/s, and 28.95g/s, respectively.

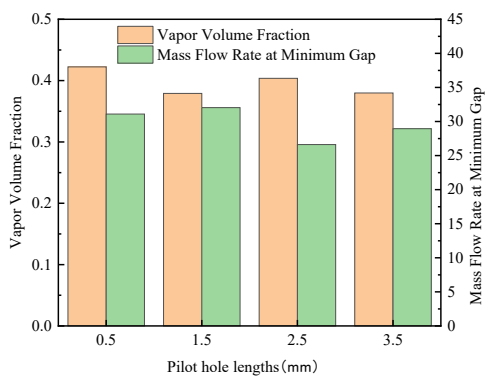


Figure 19 Mass flow rate and vapor volume fraction at the minimum gap for different pilot hole lengths

### 3.5 Effect of pilot hole diameter on cavitation

Figure 20 illustrates the cavitation cloud distribution within the ball valve for pilot hole diameters of 0.5 mm, 0.6 mm, 0.8 mm, and 1.0 mm. At a pilot hole diameter of 0.5 mm, cavitation occurs near the wall of the ball valve seat but is absent within the pilot hole. The small pilot hole

diameter restricts oil flow, increasing internal pressure and suppressing cavitation. When the pilot hole diameter increases to 0.6 mm and 0.8 mm, the cavitation region near the ball valve seat slightly diminishes, while cavitation emerges along the internal wall of the pilot hole. At 1.0 mm, cavitation intensifies in the upper ball valve region near the sealing ball and ball seat, whereas cavitation within the pilot hole vanishes entirely.

Figure 21 shows the distribution of flow velocity for the four configurations. When the diameter of the orifice is 0.5mm, the fuel's average flow velocity in the ball valve's minimum clearance section is 448.545m/s. When the diameter of the orifice is 0.6mm, the average flow velocity in the minimum clearance section of the ball valve is 551.46m/s. When the diameter of the orifice is 0.8mm, the average flow velocity in the minimum clearance section of the ball valve is 489.91m/s. When the diameter of the guide hole is 1.0mm, the average flow velocity on the minimum clearance section of the ball valve is 393.121m/s.

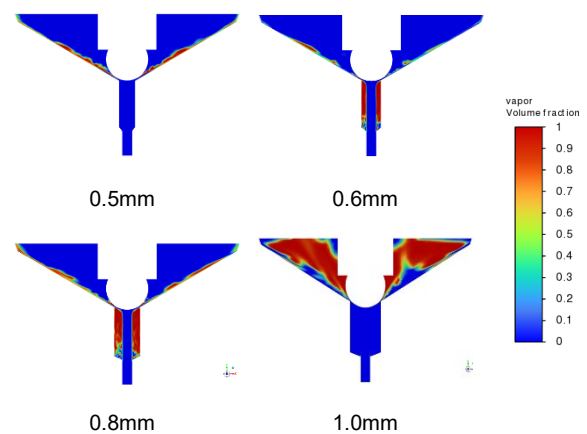
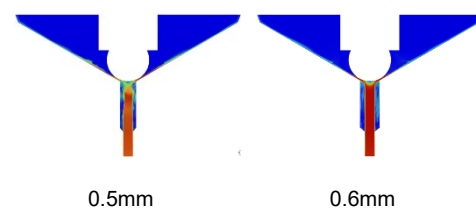


Figure 20 Effect of different guide hole diameters on cavitation





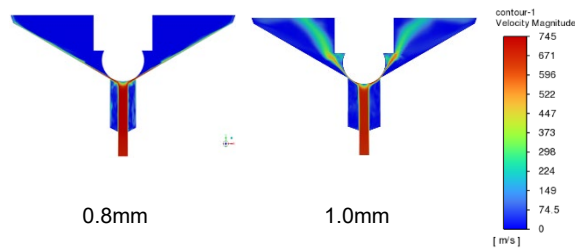


Figure 21 Flow velocity for different guide hole diameters

Figure 22 shows the effect of pilot orifice diameter on the minimum clearance mass flow rate and the gas volume fraction in the critical region of the ball valve. Both of them increase first and then decrease. The lowest gas volume fraction in the critical region is found at a pilot hole diameter of 0.06 mm, the lowest minimum clearance mass flow rate at 0.05 mm, and the highest at 0.8 mm. Specifically, the gas volume fractions in the critical region for the deflector hole diameters of 0.5 mm, 0.6 mm, 0.8 mm, and 1.0 mm are 0.151, 0.146, 0.379, and 0.158, respectively, corresponding to the minimum gap mass flow rates of 29.50 g/s, 34.01 g/s, 32.04 g/s, and 30.01 g/s.

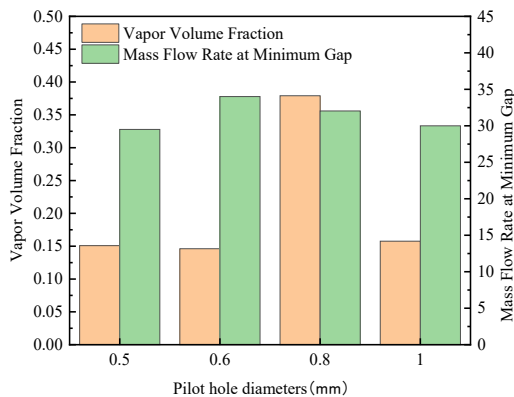


Figure 22 Mass flow rate and gas volume fraction at the minimum gap for different pilot hole diameters

### 3.6 Effect of oil supply hole length on cavitation

Figure 23 shows the cavitation cloud inside the ball valve under four oil supply hole lengths of 0.75 mm, 1.5 mm, 2.5 mm, and 5 mm. The figure shows that the cavitation region in the upper part of the ball valve tends to extend along the wall surface of the ball valve seat under the four different oil supply

hole length structures. When the length of the oil supply hole was 0.75 mm, a small part of the cavitation phenomenon appeared near the wall surface of the ball valve seat, and with the gradual increase of the length of the oil supply hole from 0.75 mm to 1.5 mm and 2.5 mm, the degree of cavitation near the wall surface of the ball valve seat tended to increase. The cavitation region near the wall surface of the ball valve seat tended to decrease again when the length of the oil supply hole was increased to 5 mm. In addition, cavitation was also observed near the wall surface in the pilot hole under all four different structures. Figure 24 shows the flow velocity distribution under the four structures. The average flow velocities at the minimum clearance cross section of the fuel ball valve were 489.91 m/s and 439.43 m/s for the oil supply hole lengths of 0.75 mm and 1.5 mm. The average flow velocities at the minimum clearance cross section of the fuel ball valve were 456.63 m/s and 518.34 m/s for the oil supply hole lengths of 2.5 mm and 5 mm.

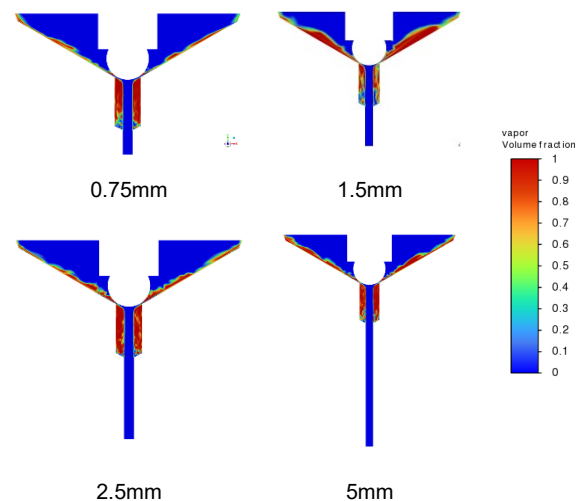
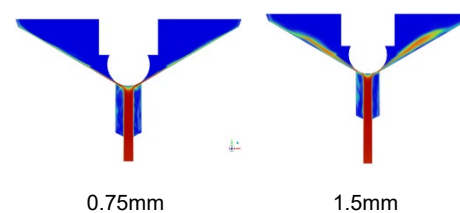


Figure 23 Cavitation pictures for different oil supply hole lengths





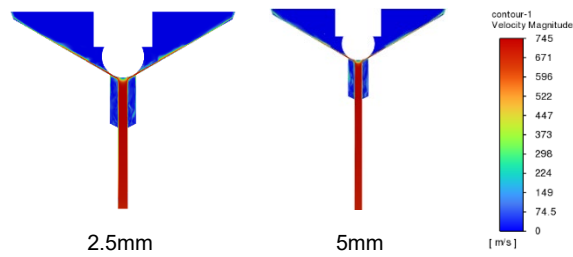


Figure 24 Flow velocity at different lengths of oil supply holes

Figure 25 shows the mass flow rate at the minimum clearance and the gas volume fraction in the critical region of the ball valve for different oil supply hole lengths. From the figure, it can be seen that the oil supply hole length has little effect on the gas volume fraction in the critical region, where the gas volume fraction in the critical region of the ball valve is the lowest at an oil supply hole length of 0.75 mm, which is 0.379. With the increase of the oil supply hole lengths to 1.5 mm and 2.5 mm, the gas volume fraction in the critical area shows an increasing trend; the gas volume fraction in the oil supply hole length of 1.5mm is 0.382, the gas volume fraction in the oil supply hole length of 2.5mm is 0.392, and the gas volume fraction in the oil supply hole length of 5mm is 0.386. mass flow rate at the gap is 26.54g/s, 31.87 g/s, and 30.59g/s, respectively.

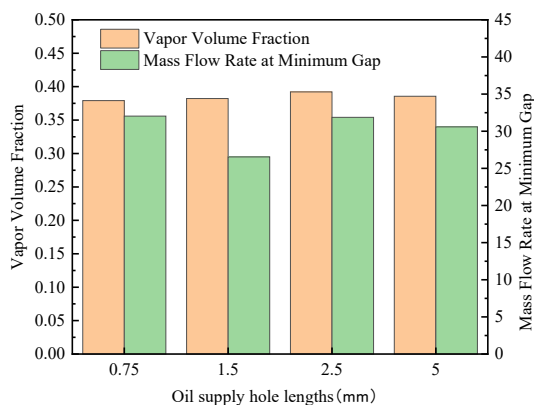


Figure 25 Mass flow rate and gas volume fraction at the minimum gap for different oil supply hole lengths

### 3.7 Optimization of structural parameters

To mitigate cavitation in the control valve and enhance its operational stability and reliability, this study employed the response surface method via

Design-Expert software to optimize the valve's structural parameters. The optimization framework incorporated six independent variables: the ball valve seat cone angle (X1), ball valve lift (X2), sealing ball diameter (X3), pilot hole length (X4), pilot hole diameter (X5), and oil supply hole length (X6). The vapor volume fraction (Y1) and outlet mass flow rate (Y2) were selected as dependent variables, with the dual objectives of minimizing cavitation (vapor volume fraction) and maximizing the outlet mass flow rate.

As summarized in Table 4, the structural parameters of the control valve before and after optimization are compared. Figure 26 illustrates the pre- and post-optimization valve geometries alongside cavitation cloud diagrams. The results demonstrate that structural optimization significantly reduced cavitation within the control valve, achieving a 65.43% reduction in vapor volume fraction at the ball valve seat sealing surface and a 3.75% increase in mass flow rate through the minimum clearance section.

Table 4 Comparison of parameters before and after optimization

	X1	X2	X3	X4	X5	X6	Y1	Y2
Before								
optimiza	120	0.05	1.3	1.5	0.8	0.75	0.379	32.04
tion								
After								
optimiza	119.8	0.044	1.32	1.84	0.53	4.04	0.129	36.35
tion								
Verificati	119.8	0.044	1.32	1.84	0.53	4.04	0.131	33.24
on								

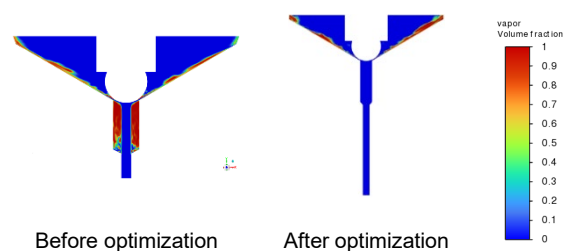


Figure 26 Comparison of structure and cavitation before and after optimization

## 4 CONCLUSION

In this study, through the establishment of a three-dimensional simulation model of the injector control valve, the influence of key structural parameters such as ball valve seat cone angle, ball valve lift, sealing ball diameter, pilot hole length, pilot hole diameter, and oil supply hole length on the internal cavitation state and flow velocity distribution of the ball valve is systematically analyzed, which reveals the important roles of these parameters on the performance of the ball valve. The results show that changes in different structural parameters can lead to significant changes in the degree of cavitation and flow velocity inside the ball valve, which in turn affects the stability and reliability of the ball valve.

Specifically, an increase in the ball valve seat cone angle causes the cavitation region to decrease and then increase, while the flow rate decreases with increasing cone angle. The increase in ball valve lift will reduce the cavitation area in the cavity, but the cavitation area near the inner wall of the guide hole increases, and the flow rate increases with the lift increase. The increase in the sealing ball diameter significantly reduces the cavitation phenomenon in the ball valve cavity and then tends to stabilize. The cavitation near the inner wall of the pilot hole gradually increases, and the flow rate increases with the increase of the sealing ball diameter. The increase in the length of the pilot hole will lead to the extension of the cavitation area along the wall of the upper part of the ball valve, and the flow velocity will be reduced due to the increase in flow resistance. Changes in the oil supply hole length have a relatively small effect on the degree of cavitation and flow velocity of the ball valve but still show a certain regularity.

In addition, the structural parameters of the control valve were optimized in this study by response surface methodology with the objectives of minimizing the gas volume fraction and maximizing the outlet mass flow rate. The optimization results show that the optimized control valve has

significantly reduced internal cavitation, reduced the gas volume fraction on the sealing surface of the ball valve seat by 65.43%, and increased the minimum clearance mass flow rate by 3.75%, thus improving its stability and reliability.

## 5 REFERENCES AND BIBLIOGRAPHY

- [1] Zhiqing Z, Zhao Z, Tan D, Zhang B, Yin Z, Cui S, et al. 2024. Multi-objective optimization of chemical reaction characteristics of selective catalytic reduction in denitrification of diesel engine using ELM-MOPSO methodology, *Energy*, 311:133386.
- [2] Han D, E J, Feng C, Han C, Kou C, Tan Y, et al. 2024. Experimental and simulation investigation on the different iron content beta zeolite for controlling the cold-start hydrocarbon emission from a gasoline vehicle, *Energy*, 294:130954.
- [3] İçingür Y, Altıparmak D. 2003. Effect of fuel cetane number and injection pressure on a DI Diesel engine performance and emissions, *Energy Conversion and Management*, 44: 389-97.
- [4] Zhiqing Z, Wang S, Pan M, Junshuai L, Lu K, Ye Y, et al. 2024. Utilization of hydrogen-diesel blends for the improvements of a dual-fuel engine based on the improved Taguchi methodology, *Energy*, 292: 130474.
- [5] Agarwal A, Dhar A, Srivastava D, Maurya R, Singh A. 2014. Effect of fuel injection pressure on diesel particulate size and number distribution in a CRDI single cylinder research engine, *Fuel*, 107: 84–9.
- [6] Guan W, He Z, Zhang L, Elseesy A, Wen L, Zhang Q, et al. 2021. Effect of asymmetric structural characteristics of multi-hole marine diesel injectors on internal cavitation patterns and flow characteristics: A numerical study, *Fuel*, 283: 119324.
- [7] Li Z, Liu Z, Chen P, Liu J, Wu J. 2022. Numerical Comparative Study of Fuel Cavitation in

Microchannels under Different Turbulence Models, *Energies*, 15: 8265.

[8] Liu Z, Li Z, Liu J, Wu J, Yu Y, Ding J. 2022. Numerical Study on Primary Breakup of Disturbed Liquid Jet Sprays Using a VOF Model and LES Method, *Processes*, 10(6): 1148.

[9] Liu J, Liu Z, Wu J, Li Z, Chen P, Gu X. 2022. Visualization experiment and numerical calculation of the cavitation evolution inside the injector ball valve, *Fuel*, 329: 125500.

[10] Saha K. 2015. Assessment of Cavitation Models for Flows in Diesel Injectors With Single- and Two-Fluid Approaches, *Journal of Engineering for Gas Turbines and Power*, 138.

[11] Winklhofer E, Philipp H, Hirsch A, Morozov A. 2000. CAVITATION AND SPRAY FORMATION IN DIESEL FLOW SITUATIONS. ILASS-Europe 2001, 17 *International Conference on Liquid Atomization and Spray Systems*, Zurich, Switzerland. DOI: 10.13140/2.1.1716.4161

[12] Ma H, Zhang T, An Q, Tao Y, Xu Y. 2021. Visualization Experiment and Numerical Analysis of Cavitation Flow Characteristics in Diesel Fuel Injector Control Valve with Different Structure Design. *Journal of Thermal Science*, 30(1):76-87.

[13] Liu J, Liu Z, Wu J, Gu X. 2022. Numerical Study on Cavitation Flow Characteristics in Diesel Fuel Injector Control Valve. *International Journal of Automotive Technology*, 23(4):881-97.

[14] Chao W, Li G, Sun Z, Wang L, Sun S, Gu J, et al. 2016. Effects of structure parameters on flow and cavitation characteristics within control valve of fuel injector for modern diesel engine. *Energy Conversion and Management*, 124:104-15.

[15] Cao T, He Z, Zhou H, Guan W, Zhang L, Wang Q. 2019. Experimental study on the effect of vortex cavitation in scaled-up diesel injector nozzles and spray characteristics, *Experimental Thermal and*

*Fluid Science*, 113: 110016.

[16] Zhang X, He Z, Wang Q, Tao X, Zhou Z, Xia X, et al. 2017. Effect of fuel temperature on cavitation flow inside vertical multi-hole nozzles and spray characteristics with different nozzle geometries, *Experimental Thermal and Fluid Science*, 91.

[17] Wang F, He Z, Liu J, Wang Q. 2015. Diesel nozzle geometries on spray characteristics with a spray model coupled with nozzle cavitating flow, *International Journal of Automotive Technology*, 16.

[18] Yu H, Goldsworthy L, Brandner P, Garaniya V. 2017. Development of a compressible multiphase cavitation approach for diesel spray modelling, *Applied Mathematical Modelling*, 45.

[19] He Z, Zhong W, Wang Q, Jiang Z, Shao Z. 2013. Effect of nozzle geometrical and dynamic factors on cavitating and turbulent flow in a diesel multi-hole injector nozzle, *International Journal of Thermal Sciences*, 70:132–43.

[20] Koukouvini P, Gavaises M, Li J, Wang L. 2016. Large Eddy Simulation of Diesel injector including cavitation effects and correlation to erosion damage, *Fuel*, 175.

[21] Dai X, Wang Z, Liu F, Wang C, Sun Q, Xu C. 2019. Simulation of throttling effect on cavitation for nozzle internal flow, *Fuel*, 243: 277-87.

[22] Molina S, Salvador FJ, Carreres M, Jaramillo D. 2014. A computational investigation on the influence of the use of elliptical orifices on the inner nozzle flow and cavitation development in diesel injector nozzles, *Energy Conversion and Management*, 79: 114–27.

[23] Chen Z, He Z, Shang W, Duan L, Zhou H, Guo G, et al. 2018. Experimental study on the effect of nozzle geometry on string cavitation in real-size optical diesel nozzles and spray characteristics, *Fuel*, 232: 562-71.

[24] Cui J, Lai H, Li J, Ma Y. 2017. Visualization of

internal flow and the effect of orifice geometry on the characteristics of spray and flow field in pressure-swirl atomizers, *Applied Thermal Engineering*, 127.